7966 Vol. 61, No. 27 / 20 September 2022 / *Applied Optics* **Research Article**

applied optics

Spectrally simplified approach for leveraging legacy geostationary oceanic observations

HENRY F. HOUSKEEPER,[1,*] STANFORD B. HOOKER,[2] AND KYLE C. CAVANAUGH[1]

[1]*Department of Geography, University of California Los Angeles, Los Angeles, California 90095, USA*
[2]*NASA Goddard Space Flight Center, Ocean Ecology Laboratory, Greenbelt, Maryland 20771, USA*
**Corresponding author: hhouskee@g.ucla.edu*

Received 30 May 2022; revised 8 August 2022; accepted 10 August 2022; posted 22 August 2022; published 15 September 2022

The use of multispectral geostationary satellites to study aquatic ecosystems improves the temporal frequency of observations and mitigates cloud obstruction, but no operational capability presently exists for the coastal and inland waters of the United States. The Advanced Baseline Imager (ABI) on the current iteration of the Geostationary Operational Environmental Satellites, termed the R Series (GOES-R), however, provides sub-hourly imagery and the opportunity to overcome this deficit and to leverage a large repository of existing GOES-R aquatic observations. The fulfillment of this opportunity is assessed herein using a spectrally simplified, two-channel aquatic algorithm consistent with ABI wave bands to estimate the diffuse attenuation coefficient for photosynthetically available radiation, K_d(PAR). First, an *in situ* ABI dataset was synthesized using a globally representative dataset of above- and in-water radiometric data products. Values of K_d(PAR) were estimated by fitting the ratio of the shortest and longest visible wave bands from the *in situ* ABI dataset to coincident, *in situ* K_d(PAR) data products. The algorithm was evaluated based on an iterative cross-validation analysis in which 80% of the dataset was randomly partitioned for fitting and the remaining 20% was used for validation. The iteration producing the median coefficient of determination (R^2) value (0.88) resulted in a root mean square difference of 0.319 m^{-1}, or 8.5% of the range in the validation dataset. Second, coincident mid-day images of central and southern California from ABI and from the Moderate Resolution Imaging Spectroradiometer (MODIS) were compared using Google Earth Engine (GEE). GEE default ABI reflectance values were adjusted based on a near infrared signal. Matchups between the ABI and MODIS imagery indicated similar spatial variability ($R^2 = 0.60$) between ABI adjusted blue-to-red reflectance ratio values and MODIS default diffuse attenuation coefficient for spectral downward irradiance at 490 nm, K_d(490), values. This work demonstrates that if an operational capability to provide ABI aquatic data products was realized, the spectral configuration of ABI would potentially support a sub-hourly, visible aquatic data product that is applicable to water-mass tracing and physical oceanography research.

https://doi.org/10.1364/AO.465491

1. INTRODUCTION

Geostationary satellites increase the temporal frequency of Earth observations by enabling resampling of targeted geographic regions at up to sub-hourly intervals. A more rapid cadence of satellite observations is advantageous, in part, because a multitude of daily images can help mitigate partial scene obstruction by clouds, and rapid resampling can reveal ephemeral processes that are obscured within daily imagery obtained using polar-orbiting satellite sensors [1]. Daily observations are satisfactory for studying mesoscale-scale processes (e.g., gulf stream meanders) whereas geostationary satellite observations with improved temporal resolution provide an opportunity to investigate more rapid (e.g., deformation-scale) phenomena, including processes that reflect the sub-daily cadence of solar illumination and tidal cycles, albeit with a caution on the spatial scale involved.

In aquatic ecosystems (including oceanic, coastal, and inland waters), short-term processes can significantly degrade water quality on sub-hourly time scales. These rapid processes can be regular and predictable, like tidal cycles, or irregular and episodic, including: (a) harmful algal blooms (HABs), wherein rapid proliferation of phytoplankton produces toxic or otherwise deleterious conditions; (b) severe storms, in which runoff or resuspension can severely degrade water clarity; (c) anthropogenic pollution, including containment spills, introduction of invasive species or noxious vegetation, and resuspension due to vessel propulsion; and (d) fluid advection, whereupon an ecosystem experiences a rapid change in water quality due to the interaction with a water mass entrained by jets, streamers, or estuarine outflows.

Geostationary satellite observations of coastal waters around the Korean peninsula became available in 2010 with the launch of the Geostationary Ocean Color Imager (GOCI), which measures eight visible (VIS) or near infrared (NIR) wave bands each hour at 0.5 km spatial resolution [2,3]. GOCI is presently the only operational sensor dedicated to ocean color research on a geostationary platform [4]. Observations from GOCI have been used to detect rapid changes in water quality, e.g., changes in phytoplankton abundance associated with advection by vertical and horizontal currents [5], plus diurnal changes in the horizontal distribution of suspended particles [6]. A successor to the GOCI imager (GOCI-II) was launched in 2019 for continuity of hourly imagery for the Korean peninsula [7]. In the coastal and inland waters of the continental United States (CONUS), there is presently no operational geostationary remote sensor designed for oceanographic applications. The Geosynchronous Littoral Imaging and Monitoring Radiometer (GLIMR) is presently scheduled to launch later this decade with the objective of collecting high-resolution, hyperspectral imagery of coastal environments at hourly intervals.

Other geostationary platforms carrying sensors that are not primarily intended for ocean color research have been successfully leveraged to obtain unique oceanographic observations. For example, the Himawari-8 meteorological satellite has provided continuous geostationary observations of the eastern hemisphere since 2015 using the Advanced Himawari Imager (AHI), a multispectral sensor with three VIS wave bands, plus three NIR to short-wave infrared (SWIR) wave bands, at 10 min intervals [8]. Operational atmospheric correction of AHI imagery produces ocean color data products [8] that have supported aquatic research, e.g., to monitor the movement of floating macroalgae [9]. The Spinning Enhanced Visible and Infrared Imagers (SEVERIs) on the geostationary Meteosat Second Generation platforms provide hourly observations of Europe and Africa [10], which have been applied to oceanographic research including the detection of coccolithophore blooms [11].

Geostationary meteorological satellites have continuously imaged the western hemisphere, including the CONUS, for 47 years. Beginning in 1975, the Geostationary Operational Environmental Satellites (GOES) have provided sub-daily observations centered over the equator of the western hemisphere to support CONUS weather monitoring. Presently, two fourth generation, termed R series (GOES-R), satellites are positioned to view the western hemisphere: GOES-16 from a more eastern orbital position (GOES-East) and GOES-17 from a more western orbital position (GOES-West). Both GOES-East and GOES-West provide redundant observations of the CONUS, which significantly mitigates the risk of data loss due to sensor degradation or failure. Data continuity is also supported by the recent and upcoming launches of two more GOES-R satellite systems in 2022 and scheduled for 2024, respectively.

GOES observations are not widely used for aquatic research, in part, because legacy GOES platforms did not have multiple ocean color wave bands. For example, the GOES-N series (beginning in 2006) contained only one wave band within the VIS domain. The Advanced Baseline Imager (ABI) was added to GOES in 2017 (i.e., the GOES-R series) to improve observations of the atmosphere, land, cryosphere, and ocean [12]. ABI provides radiance observations at 16 wave bands and resamples the CONUS at 5 min intervals with 0.5–2 km spatial resolution (at the equator) depending on the wave band [13]. ABI contains multiple enhancements to earlier GOES instruments in addition to improved spectral resolution, including decreased positioning and pointing uncertainties, as well as a lunar calibration capability [14]. A summary of the spectral characteristics for the ABI sensor is shown in Table 1, reconstructed from [13]. Although ABI contains fewer VIS wave bands than many existing or legacy ocean color sensors, ABI spectral response functions for VIS and NIR wavelengths are comparable to those of the Ocean Land Imager (OLI) sensor aboard the U.S. Geological Survey Landsat-8 platform, shown in Fig. 1, which has provided sufficient spectral information to retrieve useful water quality parameters [15,16]. Despite the increased number of spectral channels from ABI relative to earlier GOES instruments, the ABI VIS observations have also not been widely used for aquatic ecosystem research due to the absence of a band in the green domain [17], and an operational ocean color capability for ABI imagery has not been established.

Recent research has established a trajectory towards an ocean-observing capability for ABI, including the development of cloud masks compatible with the ABI spectral configuration [18], the development and validation of ABI sea surface temperature (SST) algorithms [19], and the synthesis of artificial green wave band data to produce red, green, and blue (RGB) composite imagery [20,21]. For example, a synthetic green wave band algorithm was recently applied to track the evolution of water masses in the northern Gulf of Mexico based on ABI synthetic RGB imagery [20]. The primary objective of this study is to evaluate potential aquatic applications for ABI VIS imagery, for example, by deriving an algorithm to estimate the diffuse attenuation coefficient for photosynthetically available radiation, K_d(PAR), using *in situ* data that was synthesized from neighboring higher-resolution wave bands to match the ABI spectral configuration. K_d(PAR)—which integrated the diffuse attenuation coefficient for spectral downward irradiance, $K_d(\lambda)$, across the VIS domain—is a useful parameter for comparing optical properties of different water masses [22] and is appropriate for ABI applications based on the broad

Table 1. Nominal Spectral Specifications of ABI Wave Bands, with Corresponding Spatial Resolutions [12] and Generalized Transmittance of the Atmosphere under Clear Conditions[a]

Wave Band (bandwidth) [nm]	Spatial Resolution [km]	Atmospheric Transmittance	Research Applications
470 (40)	1	High	AA
640 (100)	0.5	High	AA
860 (40)	1	High	AA & AC
1370 (30)	2	Low	N/A
1600 (60)	1	High	AC
2250 (50)	2	High	AC

[a] Potential research applications for each wave band include aquatic algorithm (AA) development and atmospheric correction (AC), unless not applicable (N/A).

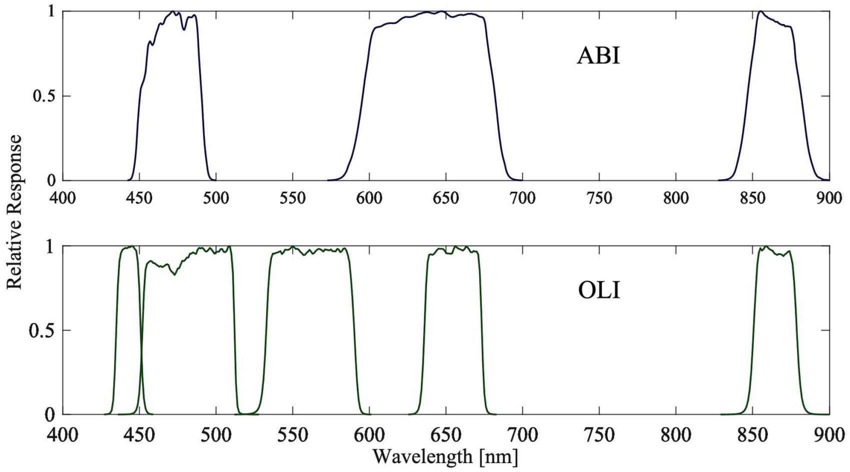

Fig. 1. Spectral response functions of the ABI (upper) and OLI (lower) sensors for VIS and NIR wave bands.

spectral response function (SRF) characteristics and low spectral resolution of the ABI instrument.

2. METHODS

A. Field Data

Aquatic field observations were used to synthesize ABI data products and evaluate ABI aquatic algorithms. An *in situ* optical dataset was obtained by deploying the Compact-Optical Profiling System (C-OPS) in oceanic, coastal, and inland water bodies [23–25]. C-OPS is a handheld profiler with a kite-shaped back plane that helps to maintain the appropriate planar and solar sensor geometry during profiling. For this study, C-OPS was routinely (97% of the time) equipped with the Compact-Propulsion Option for Profiling Systems (C-PrOPS), a digital thruster accessory that allows sampling in shallow or otherwise non-navigable waters, reduces adjacency effects, and improves surface loitering to optimize the vertical sampling resolution (VSR) of the in-water observations [26]. The mean VSR of the *in situ* data products considered herein was 6.0 mm, but the VSR was optimized based on water body characteristics including depth, stratification, and turbidity, with a VSR of 0.9 mm achieved within highly attenuating or shallow waters [23]. The C-OPS spectral configuration contained 19 wave bands spanning the ultraviolet (UV), VIS, and NIR, with 10 nm bandwidths, including wave bands centered at 465, 490, 625, and 665 nm, which were spectrally adjacent to the ABI blue and red wave bands.

The *in situ* data products evaluated herein adhered to an absolute radiometry perspective, wherein the absolute accuracy of individual corrected data products met validation requirements, i.e., 1% absolute radiometry [27], for individual wave bands [28]. For comparison, a common legacy approach in which radiometric quantities require normalization between spectral regions, i.e., radiometry in which “only the ratios of the fluxes are important,” can be described as relative radiometry [29]. Adherence of the *in situ* dataset to an absolute radiometry perspective is most succinctly demonstrated by the recent successful development of single-channel optical algorithms for aquatic remote sensing [24].

Observations were obtained from globally representative water bodies, based on approximately equal representation from oceanic, coastal, and inland waters, as well as an expansive range in bio-optical parameters. The latter included the coefficient for absorption by colored dissolved organic matter (CDOM) at 440 nm, $a_{\mathrm{CDOM}}(440)$, which exceeded three decades in dynamic range and encompassed more than 99% of global waters by surface area [24]. Prior to sampling, water bodies were classified as either conservative or nonconservative based on an objective set of criteria. The conservative classification indicated that modifications in the optical properties of a water mass were attributed to linear mixing of parent water masses, while the nonconservative classification indicated that optical properties were likely significantly influenced by internal nonlinear processes, e.g., rapid proliferation of a HAB species or continued concentration of a constituent in a drought-stricken lake [23]. The conservative criterion supports algorithm development across a continuum of oceanic, coastal, and inland waters, and its implementation has revealed that a continuous transition in optical complexity—rather than a binary complexity threshold—is applicable when describing optical properties across a global range of water bodies [16]. The *in situ* optical data products considered herein for developing the K_d(PAR) algorithm were from the conservative portion of the dataset presented by Hooker *et al*. (2020) [23], resulting in a dataset containing 766 observations. More information on the globally representative dataset, including a map of sampling locations, can be accessed in Hooker *et al*. (2020) [23].

1. Data Products Derived from the Field Dataset

The above-water data product evaluated herein for the *in situ* dataset was the normalized water-leaving radiance, $[L_W(\lambda)]_{\mathrm{N}}$, with λ representing wavelength, which was derived in a near-surface (less than 1 m) homogeneous layer and synthesized for ABI wave bands using linear interpolation of the C-OPS data products at the nearest available wave bands.

The radiometric brightening or darkening of $[L_W(\lambda)]_{\mathrm{N}}$ data products is a primary spectral mode corresponding to transitions in optical complexity for many water masses [16].

Radiometric brightness (β) was quantified by trapezoidal integration of $[L_W(\lambda)]_N$ across the relevant spectral domain as follows:

$$\beta = \sum_{i=1}^{n-1} \frac{1}{2}(\lambda_{i+1} - \lambda_i)([L_W(\lambda_i)]_N + [L_W(\lambda_{i+1})]_N), \quad \textbf{(1)}$$

wherein n denotes the number of channels with center wavelength λ, and i is an index variable.

The ratio of $[L_W(470)]_N$ over $[L_W(640)]_N$, hereafter Λ_{640}^{470}, was derived from the ABI synthesized dataset and applied as an estimator for K_d(PAR). This spectrally simplified algorithmic approach is based on end-member analysis (EMA), in which a ratio of the shortest and longest corrected wave bands (i.e., the spectral end members) relates to changes in water-mass properties [16,23–25]. EMA is based on the findings that across a global range of water bodies the dynamic range in the spectral response is highest at the spectral end members [27], and $a_{\mathrm{CDOM}}(440)$ algorithms based on the most spectrally separated data products are more robust to changes in optical complexity [23,30]. The expression of the spectral end members across clear to turbid water bodies reveals that optical complexity develops more continuously for more spectrally separated wave band ratios, which can be exploited for environmental monitoring (i.e., water-mass tracing) purposes [16].

Common optical oceanography data products were estimated using the *in situ* Λ_{640}^{470} data products, including $K_d(\lambda)$ and K_d(PAR). The latter was derived for the *in situ* dataset by integrating $K_d(\lambda)$ across the VIS domain using spectral weighting. The K_d(PAR) data product is the preferred estimand for this work because the broadband sensitivity of K_d(PAR) is useful for comparing the bio-optical properties of different water masses, e.g., due to differences in organic and inorganic particle content [22]. Evaluating K_d(PAR) is also appropriate because spectrally nonspecific data products are congruous with the broad SRF characteristics of the ABI instrument. Spectral changes in the underwater light field as a function of depth, which are relevant to deriving PAR across dissimilar depths, were not considered herein because of the focus on near-surface observations [24].

2. *Illustrative Water Body Comparisons*

Water body comparisons were selected from the global *in situ* observations—including conservative and nonconservative water bodies—by identifying pairs of related observations anticipated to share similar bio-optical properties, but for which perturbations that could potentially modify bio-optical properties (e.g., resuspension or addition of dissolved or particulate compounds) had been recorded for one of the observations in the pair. These opportunistic comparisons included scenarios wherein the state of the environment was unequivocally known before and after an event, and each optical state was sampled within a short amount of time. Six examples of water-mass modifications were analyzed, summarized as follows: (a) constituent outflow from a marsh into a large inland bay; (b) estuarine turbidity maximum within the mixing of a large estuary; (c) severe storm effects on a coastal bay; and anthropogenic events, including: (d) the consequences of a tugboat maneuvering a ship in a large channel; (e) the presence of invasive plants in a large lake; and (f) ship traffic within an inner harbor with respect to the outer harbor open to a bay.

The water body comparisons were evaluated as individual scenarios wherein optical differences between related observations were quantified based on changes in the mean values of three parameters, Λ_{640}^{470}, β, and K_d(PAR), using the absolute percent difference, ϕ:

$$\phi = 100\frac{|\bar{X} - \bar{Y}|}{\bar{Y}}, \quad \textbf{(2)}$$

where $\bar{X}$ and $\bar{Y}$ indicate the mean Λ_{640}^{470}, β, or K_d(PAR) values observed within each comparison, for the modified and reference water bodies, respectively.

3. *Cross-Validation of a K_d(PAR) Algorithm Using Synthesized ABI Data Products*

Relationships between Λ_{640}^{470} and K_d(PAR) were evaluated using a cross-validation approach with 80% of the dataset partitioned to derive model coefficients (i.e., fitting or modeling) and 20% of the dataset partitioned for evaluating the goodness-of-fit (i.e., validation). The cross-validation exercise was performed for 10,000 randomly partitioned iterations, and the median-performing result based on the coefficient of determination, R^2, is presented herein.

Uncertainty in the estimation of K_d(PAR) was evaluated using the root mean square difference (RMSD):

$$\mathrm{RMSD} = \left[\frac{1}{N_V}\sum_{i=1}^{N_V}(X_i - Y_i)^2\right]^{1/2}, \quad \textbf{(3)}$$

where i is an index variable, N_V is the number of observations in the validation data subset, and X_i and Y_i are the algorithm and observed K_d(PAR) values, respectively, from the validation data subset. RMSD is presented using raw values as well as $\log_{10}$-transformed variables, denoted RMSD-log.

B. Satellite Data

ABI imagery is available from December 2018 for three domains or tiers, depending on usage, as follows: (a) the full field of view (Full Disk); (b) U.S. waters only (CONUS); and (c) smaller targeted regions (Mesoscale). The resample rates for the three domains are approximately 10, 5, and 1 min, respectively [31]. The coverage extent for observations obtained at the GOES-West and GOES-East positions are shown in Fig. 2 for one potential configuration of the CONUS and Mesoscale domains. ABI observations can be accessed in near real time (NRT) through Google Earth Engine (GEE), with data available for analysis within 50, 25, and 20 min of the observation times for the Full Disk, CONUS, and Mesoscale domains, respectively [31].

Satellite imagery of the coastal ocean off of southern California was obtained and processed using the GEE platform [33] via the online code editor [34]. The ABI imagery used in this study was obtained from the CONUS tier of the GOES-17 ABI Level 2 Cloud and Moisture Imagery GEE repository, and

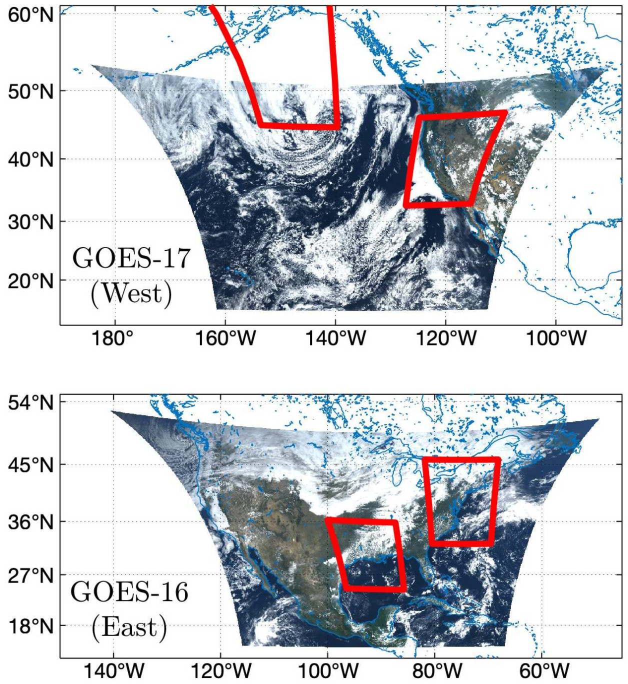

Fig. 2. GOES-R coverage for the western (upper panel) and eastern (lower panel) viewing geometries. The regions of the CONUS data products (sensed on 29 July 2021 and 2 November 2017 for the western and eastern domains, respectively) are shown as RGB pseudo-color imagery [32]. Two regions of the mesoscale data products (sensed on 1 February 2019 and 1 January 2021 for the western and eastern domains, respectively) are outlined in red. The region covered by each mesoscale domain is variable through time based on user requests.

the data products were the default GEE reflectance factor products, $\rho(\lambda)$, at VIS and NIR wave bands with a spatial resolution of 2 km [35]. Both land and clouds were masked, and $\rho(\lambda)$ values at VIS wave bands were adjusted for ocean-viewing pixels by applying an offset to the reflectance spectra so that the NIR component was equal to zero. The resulting adjusted reflectance factors, $\hat{\rho}(\lambda)$, were more appropriate for the comparisons shown herein, although the adjustment is not intended as a satisfactory substitute for an ocean-appropriate atmospheric correction. Ratios of $\hat{\rho}(470)/\hat{\rho}(640)$, hereafter ϱ_{640}^{470}, were exported from GEE for an ABI image sensed at approximately noon local time on 26 October 2021 within the region spanning 30–37°N and 116–124°W.

Imagery from the Moderate Resolution Imaging Spectroradiometer (MODIS) instrument aboard the Aqua polar-orbiting satellite platform was retrieved for the same geographic region and sensing time (within 10 min) as the ABI observations using a GEE repository containing standard mapped imagery with a resolution of 4 km [36].

MODIS $K_d(490)$ was calculated as follows:

$$K_d(490) = 10\hat{}\left[\sum_{i=0}^{4}(c_i \times b^i)\right] + 0.0166, \qquad (4)$$

where b^i is the $\log_{10}$-transformation of the ratio of remote sensing reflectances at 488 over 547 nm raised to the power of the index i, and the c_i terms are sensor-specific coefficients available in Ref. [37]. A MODIS K_d(PAR) data product was not estimated from MODIS $K_d(490)$ to minimize uncertainties related to combining multiple remote sensing algorithms.

The K_d(PAR) algorithm was not applied to the ABI observations because the default GEE ABI products had not undergone an ocean color atmospheric correction. Instead, a principal component analysis (PCA) was conducted to compare the ABI ϱ_{640}^{470} data products with the match-up MODIS Aqua $K_d(490)$ data products, after reprojecting the ABI imagery in GEE to 4 km to match the resolution of the MODIS GEE products. An ABI $K_d(490)$ data product was estimated from the ABI ϱ_{640}^{470} observations using the first PCA component in the ABI-to-MODIS comparison as a slope to transform the ABI observations. The proportion of variance in the MODIS imagery that was explained by the ABI ϱ_{640}^{470} data products was quantified using R^2 statistics of $\log_{10}$-transformed data products in the matchup imagery.

3. RESULTS

A. Water Body Comparisons Using *In Situ* Simulated ABI Data Products

The six water body comparisons are plotted based on the *in situ* synthesized $[L_W(470)]_\text{N}$ and $[L_W(640)]_\text{N}$ values, shown in Fig. 3. In all comparisons, the differences in the $[L_W(470)]_\text{N}$ and $[L_W(640)]_\text{N}$ signals correspond primarily to a radiometric brightening or darkening of the water mass, quantified herein using β [Eq. (1)]. Ocean color algorithms generally mitigate the effects of broadband brightening or darkening by using band ratios, e.g., the Λ_{640}^{470} formulation presented herein, but changes in β are included to provide an additional quantitative metric for interpreting bio-optical modifications within each water body comparison.

The percent differences among mean Λ_{640}^{470}, β, and K_d(PAR) values for the examples shown in Fig. 3 are summarized using ϕ [Eq. (2)] in Table 2 and establish three detectability parameters. The detectability parameters may be assessed by intercomparison between the scenarios, or by satisfaction of a 15% detectability threshold, chosen to match suggested uncertainty objectives for *in situ* calibration and validation activities for ocean targets to support future NASA missions [28]. The 1:1 line included in Fig. 3 demonstrates that most scenarios resulted in changes in radiometric brightness, and ϕ_β was greater than $\phi_{\Lambda_{640}^{470}}$ for all comparisons in Table 2. In other words, the primary spectral mode expressed for the water body comparisons can be summarized as broadband radiometric brightening or darkening of the water bodies, which the ABI band-ratio approach evaluated herein would most likely be insensitive to. Secondary optical modifications are detectable after mitigation of brightness differences, with $\phi_{\Lambda_{640}^{470}}$ values each greater than a 15% detectability threshold, with the exception of the harbor marine ship traffic comparison.

The $\phi_{K_d(\text{PAR})}$ values were greater than $\phi_{\Lambda_{640}^{470}}$ for all scenarios presented herein and greater than ϕ_β for all scenarios with the exception of the harbor ship traffic and estuarine tidal mixing scenarios. The relatively high responsivity of K_d(PAR) in these

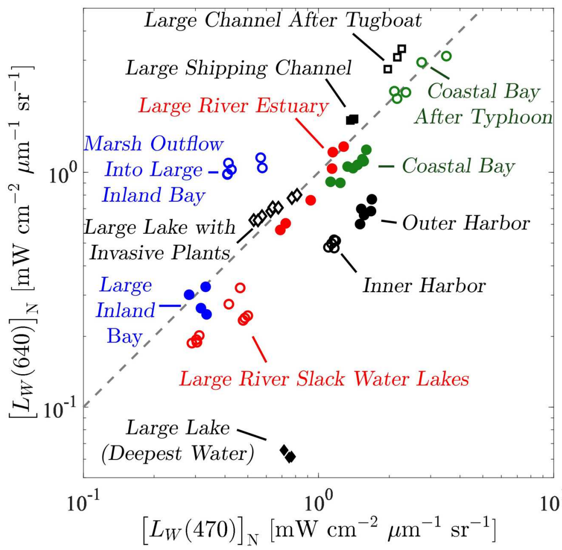

Fig. 3. Bio-optical transition scenarios observed using an in-water optical profiler. Data product wavelengths are synthesized to match the ABI spectral configuration. The environmental conditions surrounding each scenario are as follows: (a) constituent outflow from a marsh into a large inland bay (blue circles); (b) estuarine turbidity maximum within the mixing of a large estuary (red circles); (c) severe storm effects on a coastal bay (green circles); and anthropogenic events, including: (d) consequences of a tugboat maneuvering a ship in a large channel (black squares); (e) presence of invasive plants in a large lake (black diamonds); and (f) ship traffic within an inner harbor with respect to the outer harbor open to a bay (black circles).

scenarios is consistent with literature that suggests the use of K_d(PAR) for water body comparisons based on the high degree of information conferred [22]. Lower ϕ values for Λ_{640}^{470} are likely due, in part, to the reduced spectral range of the ABI sensor. For example, a prior EMA study showed that the dynamic range in $\Lambda_{\lambda_2}^{\lambda_1}$ ratios is a function of the spectral range of the band-ratio pair, and that a more spectrally expansive $\Lambda_{\lambda_2}^{\lambda_1}$ ratio provides greater sensitivity to water-mass modifications and increased loglinearity in some algorithmic relationships [23,30].

B. Estimation of K_d(PAR) from *In Situ* Synthesized ABI Data

The *in situ* Λ_{640}^{470} data products from the conservative global waters dataset were used to estimate common aquatic bio-optical parameters, including K_d(PAR). The median performing cross-validation iteration for estimating K_d(PAR) is shown in Fig. 4, with the fitting dataset indicated in gray and the validation dataset indicated in red. The algorithm residuals in the fitting and validation datasets are similar in log-space amplitude across the full range in K_d(PAR), which includes a global range of oceanic, coastal, and inland conservative water bodies. RMSD for the median-performing validation was 0.319 m^{-1}, or 8.5% of the range in the *in situ* K_d(PAR) validation dataset.

A similar algorithmic perspective was also evaluated to derive other data products, including $K_d(490)$ and $a_{\mathrm{CDOM}}(440)$, with RMSD values of 0.273 m^{-1} and 0.209 m^{-1}, or 9.9% and 10.6% of the ranges in $K_d(490)$ and $a_{\mathrm{CDOM}}(440)$, respectively, for the median-performing *in situ* validation datasets (R^2 of 0.72 and 0.87, respectively). The median R^2 value (0.88) is consistent with that of a previously published EMA approach for $a_{\mathrm{CDOM}}(440)$ estimation, which used a spectrally similar wave band ratio, i.e., Λ_{625}^{465}, that was selected to match legacy ocean color wave bands [30]. The estimation of $K_d(490)$ was slightly degraded relative to K_d(PAR) due to increased scatter in the more oligotrophic portion of the *in situ* dataset, as well as decreased loglinearity of the $K_d(490)$ relationship, which resulted in underestimation of $K_d(490)$ in the more turbid

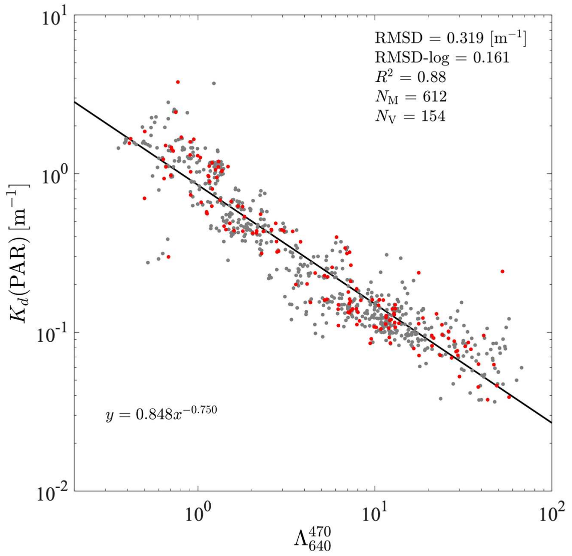

Fig. 4. Cross-validation results for estimating K_d(PAR) from observations of Λ_{640}^{470} using the *in situ* ABI dataset. The randomly selected validation and modeling (or fitting) datasets are shown in red and gray, respectively, corresponding to the cross-validation iteration (out of 10,000) that produced the median $\log_{10}$-space R^2 value. The number of observations in the validation and modeling datasets are defined as N_V and N_M, respectively.

Table 2. Differences between Mean Detectability Parameters Using Λ_{640}^{470}, β, and K_d(PAR) Values for Comparison Scenarios (Open Versus Solid Symbols) in Fig. 3

Environmental Scenario	$\phi_{\Lambda_{640}^{470}}$ [%]	ϕ_β [%]	$\phi_{K_d(\mathrm{PAR})}$ [%]	Symbol in Fig. 3
Marsh waters outflow	60.4	142.8	179.8	Blue circles
Estuarine tidal mixing	53.3	96.6	59.7	Red circles
Resuspension by typhoon	22.7	83.5	168.8	Green circles
Resuspension by tugboat	16.3	53.0	69.2	Black squares
Adjacency to invasive plants	92.2	126.8	912.7	Black diamonds
Harbor ship traffic	0.7	25.6	6.2	Black circles

portion of the *in situ* dataset, i.e., water bodies wherein $K_d(490)$ was greater than approximately 0.1 m^{-1}.

C. Estimation of $K_d(490)$ from ABI Imagery

A direct matchup between ABI and MODIS 4 km data products was evaluated by comparing coincident aquatic pixel values from mid-day imagery observed on 26 October 2021 in southern and central California. The values of the ABI band ratio ρ^{470}_{640} are compared with MODIS $K_d(490)$ values in Fig. 5, with the values for each pixel from the matchup shown in gray. A line with slope derived using the first component of the PCA is overlaid in red. Residuals to the line defined using the PCA slope are greatest in amplitude for the clearest waters, i.e., $K_d(490)$ less than 0.1 m^{-1}, with greater $K_d(490)$ values estimated on average for clear waters by MODIS. A lower prediction of $K_d(490)$ values using the ϱ^{470}_{640} approach compared to the MODIS $K_d(490)$ product was anticipated in very clear waters because the MODIS algorithm [(Eq. (4)] includes the addition of a constant, which is consistent with a pure water attenuation contribution [38], i.e., $K_w(490)$. Conversely, the lower limit in the ϱ^{470}_{640} loglinear formulation is zero, a nonphysical estimate due to the requirement that $K_d(490)$ be greater than $K_w(490)$. Adhering to the pure-water limit by adding an offset to the ABI formulation would decrease the goodness-of-fit or would require a higher-order formulation for the ABI data products. Because the goal of this analysis is to capture spatial patterns and not to minimize uncertainty in clear-water data products, the simplified loglinear approach is presented rather than a more complex, e.g., polynomial, fitting. The simplified approach is also consistent with the *in situ* cross-validation analysis, wherein no offset was applied to $[L_W(\lambda)]_\mathrm{N}$ ratios to estimate $K_d(\mathrm{PAR})$.

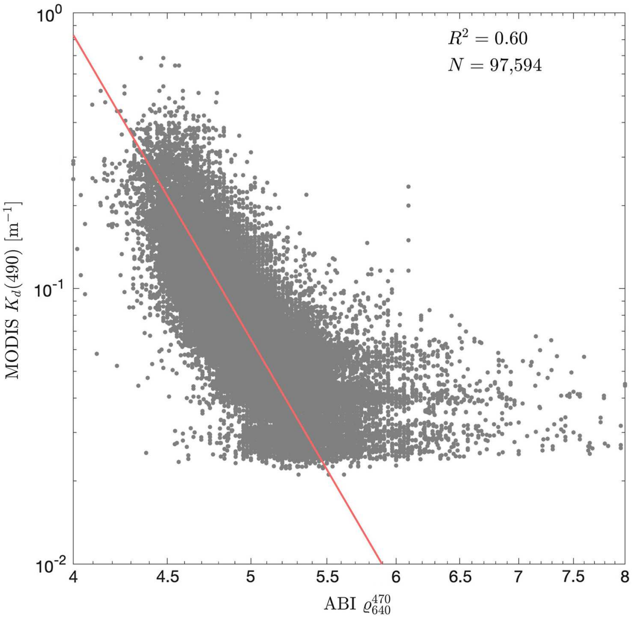

Fig. 5. Scatterplot of coincident pixel values (gray) obtained from GEE for an ABI and MODIS matchup, observed on 26 October 2021. The first principal component is overlaid in red. R^2 values were derived using $\log_{10}$-transformed variables. The number of coincident oceanic pixels is defined as N.

Future work, which should include an ocean-optimized atmospheric correction scheme for the ABI data products, could expand on the approach shown herein to improve estimation in clear waters.

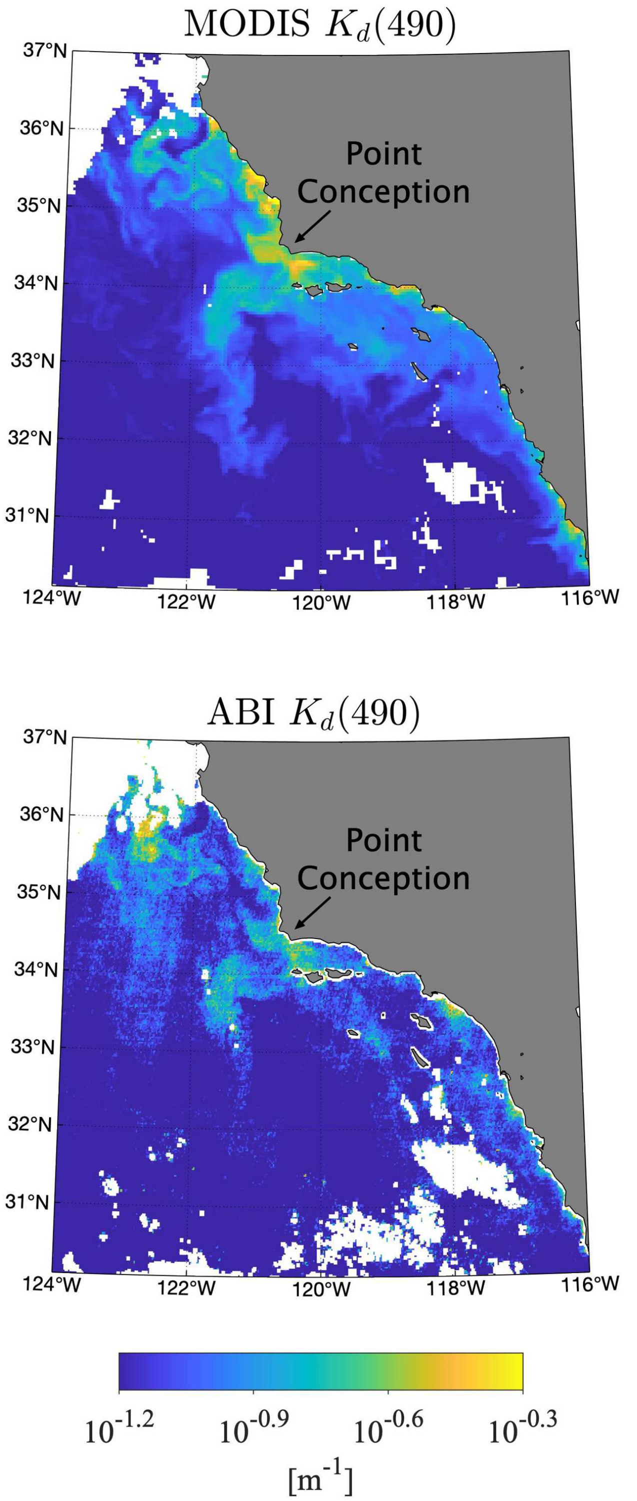

Fig. 6. Coincident MODIS (upper) and ABI (lower) imagery of estimated $K_d(490)$ in central and southern California waters, observed at mid-day on 26 October 2021. The generalized transition separating the central and southern California coastal ocean regions approximately corresponds to location of Point Conception, labeled in each panel.

Figure 6 shows a side-by-side comparison of coincident MODIS (upper panel) and ABI (lower panel) $K_d(490)$ observations. Consistent with the agreement found in Fig. 5 (i.e., $R^2 = 0.60$), the coincident MODIS and ABI images show similar spatial structures. For example, observations from both sensors reveal a jet-like structure of increased $K_d(490)$ values extending away from the Point Conception coastline in the middle of the image. Advection of coastal waters with elevated phytoplankton concentrations are common in this region, where highly productive waters fueled by coastal upwelling [39] along the central California coastline encounter an abrupt change in the coastline geometry near 34.4°N (Point Conception), where the approximately north-south coastline direction of central California gives way to the approximately east-west coastline direction in the northern portion of the Southern California Bight. The $K_d(490)$ products from the ABI and MODIS imagery also both reveal increased definition of fronts and eddies north of 34.4°N, e.g., associated with coastal upwelling common in that region, and relatively clear, low $K_d(490)$ values south of 34.4°N, where the coastline geometry decreases the prevalence or intensity of alongshore winds favorable for producing upwelling.

Increased noise in the ABI $K_d(490)$ imagery relative to the MODIS $K_d(490)$ imagery indicates that the ABI estimation is degraded in quality relative to the MODIS product, which is anticipated because the MODIS sensor is a dedicated ocean color platform with greater signal-to-noise requirements and with an ocean-optimized atmospheric correction approach. The ABI imagery sometimes shows striping effects and produces fewer pixels with high $K_d(490)$ estimates in the nearshore waters than those shown for MODIS.

4. DISCUSSION

Polar-orbiting ocean color satellites improve long-term monitoring of oceanic environments by enabling global ocean observations at approximately daily resample rates. Daily imagery is sufficient for resolving many oceanic and coastal processes. For example, decorrelation scales for phytoplankton blooms within the California Current System (CCS) are of the order of days to weeks [40]. There are numerous examples of processes that are known to occur on time scales of less than one day, particularly within dynamic coastal and inland water regions, which can result in rapid degradation of water quality. Some examples of these processes include regular diurnal and semi-diurnal tidal, atmospheric, or biological cycles, as well as sudden, ephemeral events, including containment failures or pollutant spills, plus river mouth breaching events that can inject terrestrial and riverine materials into coastal waters and significantly alter the water composition. The six example scenarios comparing optical modifications of related water masses shown in Fig. 3 resulted in ϕ values for the Λ_{640}^{470} data products that were above a 15% detectability threshold (Table 2). The time scales for the examples shown were of the orders of minutes (e.g., passage of a tugboat) to hours (e.g., tidal mixing) to days (e.g., passage of a typhoon).

Recent autonomous, aquatic-observing activities have established a trajectory towards achieving continuous, rapid sampling for global aquatic ecosystems, including sub-orbital and satellite activities. For example, *in situ* semi-autonomous systems have reached maturity, including airborne [30,41] and shipboard [42] systems, as well as a fully autonomous surface vessel [43–45]. Airborne ocean color sensors provide unique remote sensing advantages in regard to spectral, spatial, and temporal specifications—especially for coastal and inland waters [46]—but they are not the focus of this study because their sampling coverage is not comparably continuous, i.e., it is usually episodic.

Research on sub-daily processes using satellite observations is presently limited due to the sparsity of rapid-sampling spaceborne sensors with operational oceanographic capabilities. There are many opportunities to overcome this deficit, including by developing applications for small satellite constellation systems that are presently being introduced by private industry and government agencies [47,48], as well as by the development of oceanographic data processing pipelines for existing geostationary weather satellite infrastructure [8]. Observational capabilities that can match the more rapid cadence of short-term processes in ocean systems can help advance basic research on these processes and reveal situations when sub-daily processes are relevant to daily or weekly observations. For example, tidal conditions and currents alter the surface expression of kelp forest canopy, which itself does not generally vary at sub-daily rates [49]. Accounting for the effects of tides and currents for remote sensing of kelp forest ecosystems is difficult because the relationships vary in time and space. Mixing and advection patterns of coastal ocean surface waters evolve across hourly (e.g., deformation scale) to daily (e.g., mesoscale) time scales, including the formation of jets and eddies, as well as deposition from riverine pulses or ephemeral wind events.

Geostationary observations also provide potential advantages for processing oceanic data products that are enabled by resampling relatively stable targets within a single day, e.g., removal of outliers using temporal filters [4]. Operational capabilities to derive oceanic data products from existing geostationary spaceborne infrastructure would improve the redundancy of global ocean satellite observations to mitigate data losses due to cloud obstruction or in the event of a system failure or malfunction. Atmospheric correction is not the focus of this study, but NIR and SWIR ABI wave bands that are located in spectral regions with high atmospheric transmittance [13], i.e., atmospheric windows, are shown along with a comparison to MODIS channels in Fig. 7. An operational atmospheric correction for AHI observations designed to produce ocean color data products has been produced [8], and more recently, an ocean color atmospheric correction approach relevant to coastal waters was developed for both the AHI and ABI sensors based on a spectral matching method [17].

A. Development of a K_d(PAR) Algorithm for Resolving Horizontal Structure

Water-mass tracing, or the ability to distinguish between adjacent water masses with dissimilar bio-optical properties to resolve horizontal structures such as fronts and eddies, leverages the high resample rates of geostationary weather satellites, without requiring the derivation of more specific data products that are more commonly targeted by the ocean color community,

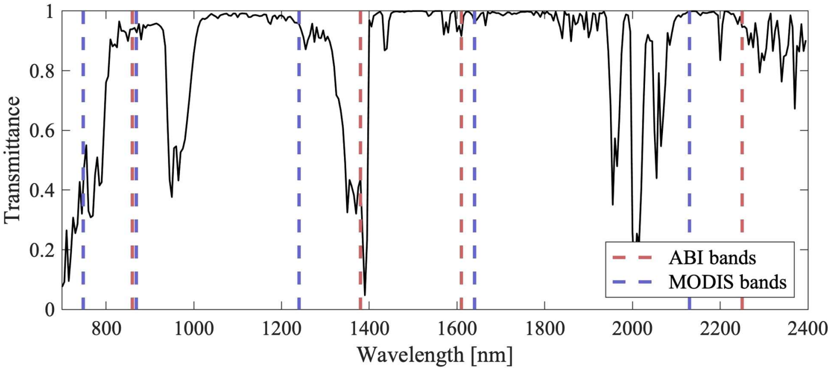

Fig. 7. Atmospheric transmittance (black), with the nominal locations of the ABI (red) and MODIS (blue) central wavelengths for the NIR and SWIR wave bands overlaid.

e.g., chlorophyll *a* (Chl *a*) or $a_{\mathrm{CDOM}}(440)$. Existing SST data products from ABI provide a useful but incomplete capability for water-mass tracing because temperature is a nonconservative parameter that may be modified by solar radiation and is generally insensitive to biological processes.

The environmental scenarios presented in Fig. 3 and Table 2 quantify the detectability of various generalized bio-optical transitions (e.g., harmful algae, ship traffic, and storm resuspension) based on the available scenarios obtained during opportunistic field sampling. The use of three detectability parameters in Table 2 ensures at least one opportunity to detect the phenomena presented. When all three parameters exceed the 15% detectability threshold, which is true for all but one of the environmental scenarios, the greater the chance the phenomenon of interest cannot be confused with an alternative explanation for spectral changes. The fact that the harbor ship traffic is detectable with only one parameter emphasizes how the flushing of the harbor into the adjoining bay continuously dilutes the episodic spectral changes created within the harbor confines.

The detectability parameters presented must also be weighed based on the observational strategies or technologies employed, as follows: the Λ^{470}_{640} data product provided decreased sensitivity compared with β or $K_d(\mathrm{PAR})$ but was applicable to a wide range of sensing perspectives, including high-altitude or spaceborne platforms because the ratio mitigates sensitivity to some atmospheric correction uncertainties; the β data product provided increased bio-optical sensitivity compared with Λ^{470}_{640} but required absolute—rather than relative—radiometry, and therefore was less applicable to high-altitude or spaceborne remote sensing requiring atmospheric correction; and the $K_d(\mathrm{PAR})$ data product provided a sensitive and informative parameter for detecting bio-optical transitions but could not be measured directly by an above-water sensor. The focus of this study is to uncover potential applications for ABI observations, and the subsequent discussion herein focuses on approaches that are consistent with the ABI spectral configuration and that mitigate inherent uncertainties associated with atmospheric correction.

The $K_d(\mathrm{PAR})$ parameter was selected as the estimand in this study because $K_d(\mathrm{PAR})$ is useful for comparing light attenuation properties between water bodies [22]. The $K_d(\mathrm{PAR})$ parameter provides a convenient data product for water-mass tracing because $K_d(\mathrm{PAR})$ captures differences in water turbidity, including those related to changes in the concentration and composition of organic and inorganic particles and the content of dissolved materials such as CDOM. In addition, $K_d(\mathrm{PAR})$ is less sensitive to spectral dependencies in $K_d(\lambda)$, which is congruent with the coarser spectral capabilities of the ABI instrument based on broad SRFs and limited spectral channels. Most importantly, although $K_d(\mathrm{PAR})$ cannot be measured directly by above-water sensors, above-water data products have been shown to enable accurate estimation of $K_d(\mathrm{PAR})$ [24]. Observations of $K_d(\mathrm{PAR})$ are also relatively common in oceanography because vertical PAR profiles are routinely measured by ocean surveys and monitoring programs, e.g., the California Cooperative Oceanic Fisheries Investigations (CalCOFI) [50]. Although $K_d(\mathrm{PAR})$ is not appropriate for all oceanographic investigations, there is no single data product that is applicable to every environmental monitoring target, and data products should be selected to match the capabilities of the sensors being utilized.

The *in situ* dataset used in the cross-validation analysis was applicable to a global range of conservative water bodies as follows: the dataset consisted of approximately equal representation from open ocean, coastal, and inland waters; and the dataset spanned a global range in CDOM absorption [16,30,45]. Rather than partitioning data based on optical complexity, i.e., case-1 versus case-2 distinctions, an objective conservative versus nonconservative categorization was assigned prior to sampling, with conservative waters defined as those resulting in a linear mixing of parent water masses [23]. The resulting $K_d(\mathrm{PAR})$ algorithm does not indicate significant log-scale nonlinearities or non-uniform residuals, and the fitting and validation datasets did not contain substantial outliers associated with coherent subsets of the conservative (generally a more expansive portion than the case-1 partition) water bodies, suggesting that an ABI $K_d(\mathrm{PAR})$ algorithm could provide a useful water-mass tracing tool without requiring regional tuning. These results are consistent with an earlier evaluation of a spectrally similar band ratio, Λ^{465}_{625}, which was evaluated for estimation of $a_{\mathrm{CDOM}}(440)$ by drones or aircraft, but which was less robust than algorithms using more spectrally expansive band ratios, e.g., Λ^{412}_{670} or Λ^{320}_{780} [30].

B. ABI and MODIS Intercomparison

Similar regional patterns in the ABI and MODIS $K_d(490)$ images were consistent with expectations of local differences in water optical properties based on the common oceanographic characteristics of the region (Section 3.C). The intercomparison agreement was based on ABI reflectance products that were intended for terrestrial—not oceanic—targets, and the $\rho(\lambda)$ spectra were adjusted by subtracting the NIR components. The $\rho(\lambda)$ adjustment improved the applicability of the default GEE ABI reflectance data products for ocean targets, but was not a substitute for an ocean-appropriate atmospheric correction. For example, VIS $\hat{\rho}(\lambda)$ data products derived for waters with nonnegligible NIR signals were likely to be significantly underestimated. Improved results would likely be obtained using an operational ABI atmospheric correction method that was intended for oceanic or aquatic targets, but no such operational capability is presently available. Recently, an ocean-optimized atmospheric correction scheme that is also relevant to more turbid coastal water types was demonstrated for ABI imagery [17] but is not operational. The absence of an operational atmospheric correction is not a detraction for this study, because the primary objective herein is to evaluate potential aquatic applications for ABI VIS imagery by evaluating spectrally simplified algorithms. A follow-on study should exploit the successes documented here and use this study as a baseline for establishing the performance of more sophisticated processing.

Horizontal striping artifacts were observed in some ABI images. Striping artifacts are common in satellite oceanography due to the relatively low signal of oceanic targets combined with calibration or solar geometry differences between detectors or due to the effects of a rotating mirror [51–54]. Solutions to removing striping artifacts from geospatial datasets include smoothing and filtering functions. Applicable destriping algorithms [54] could potentially improve the agreement between the MODIS and ABI $K_d(490)$ fields but were outside the scope of this work, which focused on evaluating potential ABI oceanographic applications and not on atmospheric correction or image post-processing.

Match-up image comparisons between MODIS and ABI were conducted near mid-day, when solar-geometry challenges to the ABI image quality, e.g., glint contamination and high air mass conditions, are generally minimized. High sensor or solar zenith angles increase the prevalence of glint contamination and complicate atmospheric correction by increasing the path length that light travels through the atmosphere [4]. The appropriate time window each day for ABI rapid-sampling observations will be determined by the capability of corrections related to solar geometry effects, combined with the temporal characteristics of available *in situ* validation datasets.

Observations obtained from geostationary orbits confer advantages for image processing as follows: atmospheric parameters or surface features within a scene can be considered temporally for quality control; sensor geometries are constant across imagery for any given target or pixel; and resample rates can be lengthened (e.g., with temporal averaging) to boost signal-to-noise parameters [4]. Other advantages are derived from the synergies between geostationary and polar-orbiting sensors. For example, high resample-rate geostationary imagery of western Europe obtained using the SEVIRI sensor was improved by normalizing data products to those obtained from match-up MODIS imagery, which had radiometric capabilities that were more suitable for ocean color research [55]. Additional applications that combine geostationary and polar-orbiting observations should be explored further, including the potential to use water-mass tracing data products observed by geostationary sensors, e.g., K_d(PAR), for temporal interpolation between same-day imagery from separate ocean color sensors.

5. CONCLUSION

A spectrally simplified algorithm compatible with the ABI spectral configuration was found to produce robust estimation of K_d(PAR), as well as other common optical oceanographic data products including $K_d(490)$ and $a_{\mathrm{CDOM}}(440)$, across a globally representative *in situ* dataset. The K_d(PAR) data product provides a convenient and informative parameter for comparing water body properties [22] and was selected for this work because of its anticipated utility for water-mass tracing. K_d(PAR) is sensitive to changes in water turbidity related to organic and inorganic particle loading, but is relatively insensitive to finer spectral dependencies in $K_d(\lambda)$ that are unlikely to be resolved using a spectrally limited sensor such as ABI. Cross-validation analysis indicated that a ratio of *in situ* ABI VIS data products was strongly associated with K_d(PAR), with a median R^2 value of 0.88 and an RMSD value constituting 8.5% of the range in the K_d(PAR) validation dataset. The results suggest that advancements in ABI processing for aquatic remote sensing could support a water-mass tracing capability based on an EMA estimation of K_d(PAR) using ABI VIS wave bands.

Coincident imagery from MODIS and ABI indicated that spatial features observed in the ABI ϱ_{640}^{470} data products were similar to those observed in the MODIS $K_d(490)$ data products, with an R^2 value of 0.60. Potential improvements to the quality of the ABI data products, specifically the application of an ocean-appropriate atmospheric correction [17] or the removal of striping artifacts [54], were not applied for the purposes of this work, but would likely result in increased correlation between the MODIS and ABI data products. The findings presented herein indicate that the ABI sensor could provide useful rapid resampling imagery of aquatic ecosystems in the coastal zone. An operational atmospheric correction methodology focused on retrieving oceanic data products, e.g., $[L_W(\lambda)]_{\mathrm{N}}$, would help realize this objective. Continuing the approach used in this study of accessing and processing imagery in a cloud-based environment, e.g., GEE, would be beneficial for ensuring low latency times and open-source transparency, and decreasing computing requirements for a broader user base.

Funding. National Aeronautics and Space Administration (NASA), as part of planning for the Aerosol, Cloud, Ecosystems (ACE) satellite mission; National Science Foundation through the Santa Barbara Long Term Ecological Research (SBC LTER) network (OCE 0620276, OCE 1232779).

Acknowledgment. This work was improved by contributions from multiple scientists who participated in related laboratory, field, or remote research campaigns, or who provided valuable feedback on the manuscript, including (in alphabetical order): J. Brown, K. Cavanaugh, L. Guild, T. Hirawake, R. Kudela, R. Lind, J. Morrow, K. Negrey, K. Suzuki, Y. Yamashita, and G. Zheng.

Disclosures. The authors declare no conflicts of interest.

Data availability. Data underlying the *in situ* results presented in this paper are not publicly available at this time. Satellite data underlying the results presented in this paper are available via Ref. [34].

REFERENCES

1. D. Antoine, "Ocean-colour observations from a geostationary orbit," Tech. Rep. 12 (International Ocean-Colour Coordinating Group (IOCCG), 2012).
2. J.-K. Choi, Y. J. Park, J. H. Ahn, H.-S. Lim, J. Eom, and J.-H. Ryu, "GOCI, the world's first geostationary ocean color observation satellite, for the monitoring of temporal variability in coastal water turbidity," J. Geophys. Res.: Oceans **117** , C09004 (2012).
3. J.-H. Ryu, H.-J. Han, S. Cho, Y.-J. Park, and Y.-H. Ahn, "Overview of Geostationary Ocean Color Imager (GOCI) and GOCI data processing system (GDPS)," Ocean Sci. J. **47**, 223–233 (2012).
4. K. Ruddick, G. Neukermans, Q. Vanhellemont, and D. Jolivet, "Challenges and opportunities for geostationary ocean colour remote sensing of regional seas: a review of recent results," Remote Sens. Environ. **146**, 63–76 (2014).
5. C. Huang, K. Shi, H. Yang, Y. Li, A.-x. Zhu, D. Sun, L. Xu, J. Zou, and X. Chen, "Satellite observation of hourly dynamic characteristics of algae with Geostationary Ocean Color Imager (GOCI) data in Lake Taihu," Remote Sens. Environ. **159**, 278–287 (2015).
6. X. He, Y. Bai, D. Pan, N. Huang, X. Dong, J. Chen, C.-T. A. Chen, and Q. Cui, "Using geostationary satellite ocean color data to map the diurnal dynamics of suspended particulate matter in coastal waters," Remote Sens. Environ. **133**, 225–239 (2013).
7. J.-H. Ahn and Y.-J. Park, "Estimating water reflectance at near-infrared wavelengths for turbid water atmospheric correction: a preliminary study for GOCI-II," Remote Sens. **12**, 3791 (2020).
8. H. Murakami, "Ocean color estimation by Himawari-8/AHI," Proc. SPIE **9878**, 177–186 (2016).
9. X. Chen, S. Shang, Z. Lee, L. Qi, J. Yan, and Y. Li, "High-frequency observation of floating algae from AHI on Himawari-8," Remote Sens. Environ. **227**, 151–161 (2019).
10. E. J. Kwiatkowska, K. Ruddick, D. Ramon, Q. Vanhellemont, C. Brockmann, C. Lebreton, and H. G. Bonekamp, "Ocean colour opportunities from Meteosat second and third generation geostationary platforms," Ocean Sci. **12**, 703–713 (2016).
11. Q. Vanhellemont, G. Neukermans, and K. Ruddick, "High frequency measurement of suspended sediments and coccolithophores in European and African coastal waters from the geostationary SEVIRI sensor," *Proceedings of the EUMETSAT Meteorological Satellite Conference & 19th American Meteorological Society (AMS) Satellite Meteorology, Oceanography, and Climatology Conference*, Vienna, Austria, 2013, vol. **1620**.
12. T. J. Schmit, S. S. Lindstrom, J. J. Gerth, and M. M. Gunshor, "Applications of the 16 spectral bands on the Advanced Baseline Imager (ABI)," J. Oper. Meteorol. **6**, 33–46 (2018).
13. T. J. Schmit and M. M. Gunshor, "Chapter 4—ABI imagery from the GOES-R series," in *The GOES-R Series*,S. J. Goodman, T. J. Schmit, J. Daniels, and R. J. Redmon, eds. (Elsevier, 2020), pp. 23–34.
14. S. Kalluri, C. Alcala, J. Carr, P. Griffith, W. Lebair, D. Lindsey, R. Race, X. Wu, and S. Zierk, "From photons to pixels: processing data from the Advanced Baseline Imager," Remote Sen. **10**, 177 (2018).
15. B. A. Franz, S. W. Bailey, N. Kuring, and P. J. Werdell, "Ocean color measurements with the operational land imager on Landsat-8: implementation and evaluation in SeaDAS," J. Appl. Remote Sens. **9**, 096070 (2015).
16. S. B. Hooker, H. F. Houskeeper, R. M. Kudela, A. Matsuoka, K. Suzuki, and T. Isada, "Spectral modes of radiometric measurements in optically complex waters," Cont. Shelf Res. **219**, 104357 (2021).
17. B.-C. Gao and R.-R. Li, "Improving water leaving reflectance retrievals from ABI and AHI data acquired over case 2 waters from present geostationary weather satellite platforms," Remote Sens. **12**, 3257 (2020).
18. A. K. Heidinger, M. J. Pavolonis, C. Calvert, J. Hoffman, S. Nebuda, W. Straka, III, A. Walther, and S. Wanzong, "ABI cloud products from the GOES-R series," in *The GOES-R Series* (Elsevier, 2020), pp. 43–62.
19. B. Petrenko, A. Ignatov, N. Shabanov, and Y. Kihai, "Development and evaluation of SST algorithms for GOES-R ABI using MSG SEVIRI as a proxy," Remote Sens. Environ. **115**, 3647–3658 (2011).
20. J. K. Jolliff, M. D. Lewis, S. Ladner, and R. L. Crout, "Observing the ocean submesoscale with enhanced-color GOES-ABI visible band data," Sensors **19**, 3900 (2019).
21. D. T. Lindsey, S. D. Miller, and C. Seaman, "Red-green-blue composites from the GOES-R series ABI," in *The GOES-R Series* (Elsevier, 2020), pp. 35–42.
22. J. T. Kirk, *Light and Photosynthesis in Aquatic Ecosystems* (Cambridge University, 1994).
23. S. B. Hooker, A. Matsuoka, R. M. Kudela, Y. Yamashita, K. Suzuki, and H. F. Houskeeper, "A global end-member approach to derive aCDOM(440) from near-surface optical measurements," Biogeosciences **17**, 475–497 (2020).
24. S. B. Hooker, H. F. Houskeeper, R. N. Lind, and K. Suzuki, "One- and two-band sensors and algorithms to derive aCDOM(440) from global above- and in-water optical observations," Sensors **21**, 5384 (2021).
25. H. F. Houskeeper, *Advances in Bio-Optics for Observing Aquatic Ecosystems* (University of California, 2020).
26. S. B. Hooker, R. N. Lind, J. H. Morrow, J. W. Brown, K. Suzuki, H. F. Houskeeper, T. Hirawake, and E. d. R. Maúre, "Advances in above-and in-water radiometry, volume 1: enhanced legacy and state-of-the-art instrument suites," Tech. Rep. (National Aeronautics and Space Administration, 2018).
27. S. B. Hooker, J. H. Morrow, and A. Matsuoka, "Apparent optical properties of the Canadian Beaufort Sea–part 2: the 1% and 1 cm perspective in deriving and validating AOP data products," Biogeosciences **10**, 4511–4527 (2013).
28. S. B. Hooker, C. R. McClain, and A. Mannino, "A comprehensive plan for the long-term calibration and validation of oceanic biogeochemical satellite data," NASA Special Pub. 2007–214152 (National Aeronautics and Space Administration, 2007).
29. J. Geist, "Fundamental principles of absolute radiometry and the philosophy of this NBS program (1968 to 1971)," Tech. Rep. (National Bureau of Standards, 1972).
30. H. F. Houskeeper, S. B. Hooker, and R. M. Kudela, "Spectral range within global aCDOM(440) algorithms for oceanic, coastal, and inland waters with application to airborne measurements," Remote Sens. Environ. **253**, 112155 (2021).
31. J. Braaten, "GOES in Earth engine," (2021), https://jstnbraaten.medium.com/goes-in-earth-engine-53fbc8783c16.
32. M. Bah, M. Gunshor, and T. Schmit, "Generation of GOES-16 true color imagery without a green band," Earth Space Sci. **5**, 549–558 (2018).
33. N. Gorelick, M. Hancher, M. Dixon, S. Ilyushchenko, D. Thau, and R. Moore, "Google Earth Engine: planetary-scale geospatial analysis for everyone," Remote Sens. Environ. **202**, 18–27 (2017).
34. Google earth engine code editor, https://code.earthengine.google.com.
35. NOAA, "GOES-17 MCMIPC series ABI level 2 cloud and moisture imagery CONUS," NOAA (2018), https://developers.google.com/earth-engine/datasets/catalog/NOAA_GOES_17_MCMIPC.
36. NASA, "Ocean color SMI: standard mapped image MODIS aqua data," NASA OB.DAAC at NASA Goddard Space Flight Center (2002), https://developers.google.com/earth-engine/datasets/catalog/NASA_OCEANDATA_MODIS-Aqua_L3SMI.
37. NASA's OceanColor Web, https://oceancolor.gsfc.nasa.gov.
38. A. Morel and S. Maritorena, "Bio-optical properties of oceanic waters: a reappraisal," J. Geophys. Res.: Oceans **106**, 7163–7180 (2001).
39. D. M. Checkley, Jr. and J. A. Barth, "Patterns and processes in the California Current System," Prog. Oceanogr. **83**, 49–64 (2009).
40. S. Frolov, R. M. Kudela, and J. G. Bellingham, "Monitoring of harmful algal blooms in the era of diminishing resources: a case study of the U.S. west coast," Harmful Algae **21**, 1–12 (2013).
41. L. S. Guild, R. M. Kudela, S. B. Hooker, S. L. Palacios, and H. F. Houskeeper, "Airborne radiometry for calibration, validation, and research in oceanic, coastal, and inland waters," Front. Environ. Sci. **8**, 585529 (2020).

42. E. Boss, M. Picheral, T. Leeuw, A. Chase, E. Karsenti, G. Gorsky, L. Taylor, W. Slade, J. Ras, and H. Claustre, "The characteristics of particulate absorption, scattering and attenuation coefficients in the surface ocean; contribution of the Tara oceans expedition," Methods Oceanogr. **7**, 52–62 (2013).
43. S. B. Hooker, R. N. Lind, J. H. Morrow, J. W. Brown, R. M. Kudela, H. F. Houskeeper, and K. Suzuki, "Advances in above-and in-water radiometry, volume 2: autonomous atmospheric and oceanic observing systems," Tech. Rep. (National Aeronautics and Space Administration, 2018).
44. S. B. Hooker, R. N. Lind, J. H. Morrow, J. W. Brown, R. M. Kudela, H. F. Houskeeper, and K. Suzuki, "Advances in above-and in-water radiometry, volume 3: hybridspectral next-generation optical instruments," Tech. Rep. (National Aeronautics and Space Administration, 2018).
45. S. B. Hooker, H. F. Houskeeper, R. N. Lind, R. M. Kudela, and K. Suzuki, "Verification and validation of hybridspectral radiometry obtained from an unmanned surface vessel (USV) in the open and coastal oceans," Remote Sens. **14**, 1084 (2022).
46. R. M. Kudela, S. B. Hooker, H. F. Houskeeper, and M. McPherson, "The influence of signal to noise ratio of legacy airborne and satellite sensors for simulating next-generation coastal and inland water products," Remote Sens. **11**, 2071 (2019).
47. M. Safyan, "Planet's Dove Satellite constellation," in *Handbook of Small Satellites: Technology, Design, Manufacture, Applications, Economics and Regulation* (2020), pp. 1–17.
48. A. Holmes, J. M. Morrison, G. Feldman, F. Patt, and S. Lee, "Hawkeye ocean color instrument: performance summary," Proc. SPIE **10769**, 107690C (2018).
49. K. C. Cavanaugh, T. Bell, M. Costa, *et al.*, "A review of the opportunities and challenges for using remote sensing for management of surface-canopy forming kelps," Front. Mar. Sci. **8**, 753531 (2021).
50. California Cooperative Fisheries Investigations, https://calcofi.com/.
51. M. Bouali and A. Ignatov, "Adaptive reduction of striping for improved sea surface temperature imagery from Suomi national polar-orbiting partnership (S-NPP) visible infrared imaging radiometer suite (VIIRS)," J. Atmos. Ocean. Technol. **31**, 150–163 (2014).
52. X. Geng, A. Angal, J. Sun, A. Wu, T. Choi, and X. Xiong, "Characterization of MODIS mirror side difference in the reflective solar spectral region," Proc. SPIE **8153**, 81531O (2011).
53. Q. Liu, C. Cao, and F. Weng, "Striping in the Suomi NPP VIIRS thermal bands through anisotropic surface reflection," J. Atmos. Ocean. Technol. **30**, 2478–2487 (2013).
54. K. Mikelsons, M. Wang, L. Jiang, and M. Bouali, "Destriping algorithm for improved satellite-derived ocean color product imagery," Opt. Express **22**, 28058–28070 (2014).
55. Q. Vanhellemont, G. Neukermans, and K. Ruddick, "Synergy between polar-orbiting and geostationary sensors: remote sensing of the ocean at high spatial and high temporal resolution," Remote Sens. Environ. **146**, 49–62 (2014).